Journal of Cluster Science (2026) 37:64
https://doi.org/10.1007/s10876-026-03019-w

ORIGINAL PAPER

Green Synthesis and Characterization of NiO Nanoparticles using Kenger Gum: Evaluation of Antimicrobial, Antibiofilm and Anticancer Properties

Zehra Çiçek[1] · Güney Gürsoy[2] · Esen Çakmak[3] · Saniye Tekerek[4] · Esin Kiray[5] · Ayça Tanriverdi[4]

Received: 21 November 2025 / Accepted: 7 April 2026 / Published online: 20 April 2026

Abstract

In this study, it was aimed to determine the characterization properties of Nickel Oxide nanoparticles (NiO NPs) obtained by green synthesis method using gum Kenger along with their antimicrobial, antibiofilm and anticancer potentials. The morphological and crystalline properties related to the characterization of the obtained NiO NPs were determined by X-ray diffraction (XRD), field emission scanning electron microscope (FE-SEM), UV-visible spectroscopy (UV-vis), Fourier transform infrared spectroscopy (FT-IR) methods. Thermal properties of the NPs were analyzed by Thermogravimetric analysis (TGA, Differential thermal analysis) (DTA) and Derivative Thermogravimetry (DTG). Antimicrobial, antibiofilm tests were performed to evaluate the biological activities of NiO NPs. The anticancer activity of NPs was determined in human neuroblastoma cell line (SH-SY5Y) by cell viability (MTT assay), caspase-3 (Caspase-3/CPP32 Fluorometric Assay), apoptosis/necrosis and cell cycle (Flow cytometry assay) analyses. The crystal structure of the synthesized nanoparticles was confirmed in XRD analysis. FE-SEM analysis revealed that the particle size distribution of NiO NPs predominantly ranged from 20 to 50 nm.When evaluated in terms of biological activities, the obtained NiO NPs were found to be effective against multidrug-resistant bacteria, which have increased in recent years. It exhibited strong antimicrobial activity especially against clinically important strains such as *E. coli*, *P. aeruginosa*, *A. baumannii* and *S. aureus*. In cytotoxicity assays carried out on SH-SY5Y neuroblastoma cell line, NiO NPs decreased cell viability dose-dependently and the IC_{50} value was calculated as 23.26 ± 0.59 µg/mL. Cell cycle assays showed that NiO NPs arrested cells in G0/G1 phase and accordingly suppressed cell proliferation. No significant change was detected in caspase-3 activity, which is an apoptosis marker. However, in apoptosis/necrosis assay, a dose-dependent increase was observed, especially in the rate of necrotic cells. These findings indicate that green synthesized NiO NPs, with their structural properties, may be among the biological agents with strong antimicrobial, antibiofilm and anticancer potential.

Keywords Nanoparticles · Green synthesis · Antimicrobial · Anticancer · Apoptosis/necrosis

✉ Güney Gürsoy
guneygursoy@ahievran.edu.tr

Zehra Çiçek
zehra.cicek@sbu.edu.tr

Esen Çakmak
esencakmak@ksu.edu.tr

Saniye Tekerek
saniyetekerek@ksu.edu.tr

Esin Kiray
esin.kiray@ahievran.edu.tr

Ayça Tanriverdi
aycatanriverdi@ksu.edu.tr

[1] Department of Physiology, Gülhane Faculty of Medicine, University of Health Sciences, Ankara, Türkiye

[2] Department of Biophysics, Department of Basic Medical Sciences, Faculty of Medicine, Kırsehir Ahi Evran University, Kırsehir, Türkiye

[3] Department of Bioengineering and Sciences, Graduate School of Natural and Applied Sciences, Kahramanmaras Sütcü Imam University, Kahramanmaras, Türkiye

[4] Department of Material Science and Engineering, Graduate School of Natural and Applied Sciences, Kahramanmaras Sütcü Imam University, Kahramanmaras, Türkiye

[5] Department of Medical Services and Techniques, Medical Laboratory Techniques Program, Vocational School of Health Services, Kırsehir Ahi Evran University, Kırsehir, Türkiye

Introduction

Traditionally, Nickel Oxide nanoparticles (NiO NPs) have been synthesized using various chemical, physical, and biological methods. Chemical precipitation, sol-gel, hydrothermal, and microwave-assisted methods are among the most commonly employed conventional techniques for synthesizing metal oxide nanoparticles [1]. These methods often require the use of toxic chemicals, high temperatures, and extensive energy consumption, which raises environmental concerns.In contrast, green synthesis techniques have emerged as a sustainable alternative to traditional nanoparticle production methods. Natural products, as sustainable and environmentally friendly sources of biologically active compounds, have constituted an important area in nanotechnology and biomedical research in recent years.Green synthesis utilizes environmentally friendly materials, such as plant extracts, bacteria, fungi, and other natural agents, to reduce metal ions and stabilize nanoparticles [2]. The advantages of green synthesis includecost-effectiveness, simplicity, and the use of non-toxic and biodegradable materials, making it a more eco-friendly alternative to conventional method [3]. Plant-based synthesis, in particular, has become increasingly popular due to its numerous advantages, such as the wide availability of plant resources, low toxicity, and ease of handling [4].

Kenger gum, a natural resin obtained from the *Gundelia tournefortii L*. plant, has been traditionally used for food and medicinal purposes in the Eastern Anatolia Region of Turkey.*G. tournefortii L*. is a species that spreads in the temperate climate zone of Western Asia and grows naturally in countries such as Turkey, Cyprus, Turkmenistan, Egypt and Israel [5–7].Different parts of the *G. tournefortii* plant, including the stem, leaves, flowers, and gum obtained from its latex, are used in traditional medicine to treat a wide range of ailments, from gastrointestinal disorders and diabetes to bronchitis, inflammation, and pain. Research indicates that G. Tournefortii is rich in biologically active compounds, including phenolic acids, flavonoids, terpenoids, sterols, fatty acids, and minerals [8–11]. The presence of particularly high phenolic and flavonoid content underlies the plant's strong antioxidant capacity, contributing to its wide range of biological activity, including antioxidant, anti-inflammatory, hepatoprotective, antidiabetic, antimicrobial, and anticancer effects [12–15].These biological activities are associated with the plant's rich phenolic content and secondary metabolites, supporting the evaluation of *G. tournefortii* as a remarkable and promising resource for nanotechnological applications carried out on the basis of environmentally friendly approaches.

Although NiO NPs obtained using different plant extracts via green synthesis methods have been widely reported in the literature, these studies mainly rely on aqueous leaf and flower extracts as reducing agents. In contrast, Kenger gum is a latex-derived plant secretion with a unique biochemical composition, particularly rich in polysaccharides and phenolic compounds. These components may enable Kenger gum to function not only as a reducing agent but also as an effective stabilization and coating material during nanoparticle formation. To our knowledge, the use of Kenger gum in the green synthesis of NiO NPs has not been previously reported.

In this study, NiO NPs were obtained by green synthesis method using Kenger gum; these NPs were analyzed by various characterization techniques and their antimicrobial, antibiofilm and anticancer activities were evaluated in detail. The aim of the study is to synthesize biocompatible NPs with an environmentally friendly method and to reveal the biological potential of Kenger gum with nanotechnological applications.

Experimental Method

Materials

The chemicals used in the experimental studies were analytical grade and distilled water was used to prepare all solutions. The salt of nickel (II) chloride ($NiCl_2.6H_2O$) was purchased from Sigma. Kenger gum was purchased commercially.

Green Synthesis of NiO NPs

In this study, NiO NPs were synthesized via a green synthesis approach using Kenger gum as a natural biopolymer source. Initially, 3 g of Kenger gum were dispersed in 100 mL of distilled water to prepare a stock solution, which was magnetically stirred at 40 °C for 2 h to ensure homogeneous extraction of bioactive components. The pH of the resulting Kenger gum extract was measured and found to be 6.7. Subsequently, 1.6 g of nickel(II) chloride hexahydrate ($NiCl_2 \cdot 6\ H_2O$) was added directly to the prepared stock solution, and the reaction mixture was incubated at 75 °C for an additional 24 h under continuous stirring to facilitate complexation and nanoparticle formation. Following the addition of $NiCl_2$, the pH of the reaction mixture slightly decreased and was recorded as 6.4.No external pH adjustment was applied during the synthesis, and the reaction proceeded under the natural pH conditions of the gum extract.After completion of the reaction, the formed precipitate was

separated by centrifugation at 4000 rpm for 10 min [16]. The collected solid was washed three times with distilled water to remove unreacted species and residual impurities, followed by drying at room temperature. Finally, the dried precursor powder was calcined at anannealing temperature of 450 °C for 2 h, which was selected to ensure complete thermal decomposition of organic constituents and to achieve the formation of crystalline NiO without inducing particle agglomeration, in accordance with previously reported literatüre [17].

Characterization

The NPs were structurally characterized by recording the X-ray diffraction patterns using a Rigaku SmartLab advanced X-ray diffraction (XRD) system with CuKα (0.154 nm) radiation.Surface morphology of NP was investigated by Zeiss Supra 55 field emission scanning electron microscopy (FE-SEM). The absorption spectra of the NPs were obtained with a UV-Vis spectrophotometer (Shimadzu UV-2600). The chemical composition and functional groups of the NPs were examined using the PerkinElmer/MID-Spectrum Two/UATR FTIR instrument.

Antimicrobial Activity

Agar well diffusion method was used to determine the antimicrobial activity of newly synthesized NiONPs. Both strains isolated from clinical samples and standard strains were used in the antimicrobial activity study. *Escherichia coli*ATCC 25,922, *Pseudomonas aeruginosa*ATCC 27,853, *Staphylococcus aureus* ATCC 25,923, *Acinetobacter baumannii*ATCC 17,978, *Enterococcus faecalis* ATCC 29,212, *Enterobacter aerogenes* ATCC 13,048, *Listeria monocytogenes* ATCC 19,115, *Shigella dysentery* ATCC 13,313 and *Bacillus cereus* ATCC 14,579 were used as standard strains in the study, while *Klebsiella pneumoniae* and Vancomycin-resistant *Enterococcus faecium* (VRE) were used as clinical isolates. Cultures grown in Tryptic Soy Broth (TSB) at 37 ° C for 18 h were transferred to Tryptic Soy Agar (TSA) medium as 100 µL (0.5 Mc Farland) and inoculation was performed without leaving any gaps on the medium. 100 µL of 100 mg/mL concentration of NiONPs was added to the wells (6 mm) opened on the medium. Cultures were incubated at 37 ° C for 24 h to determine the zone diameters formed around the wells. The negative control was sterile water that had been distilled. By measuring the width of the inhibitory zone in millimeters, antimicrobial activity was measured. For the purpose of calculating antimicrobial activity, the average of three separate investigations was used [18].

Determination of Minimum Inhibitory Concentration (MIC)

The Clinical and Laboratory Standards Institute broth microdilution technique was adapted to measure the minimum inhibitory concentration (MIC). In 96-well plates using TSB medium, all antimicrobial effectiveness study isolates' MICs were determined. Cultures were diluted to 1×10^6 CFU/mL and 50 µL of bacteria were added to each well after overnight incubation at 37 °C. We incubated freshly synthesized NiONPs in a 96-well plate at 37 °C for 18 h at concentrations ranging from 256 to 0.5 µg/mL in 50 µL. Minimum concentration at which no observable bacterial growth occurred was MIC. Positive control: Gentamicin (Sigma Aldrich, USA) [19].

Anti-biofilm Activity

The anti-biofilm activity of the produced NiONPs was assessed using strains of *P. aeruginosa* ATCC 27,853 and *E. coli* ATCC 25,922, which produce biofilms. Following serial dilutions, 100 mL of bacterial culture (OD 600 = 0.132) activated in TSB medium at 37 °C and 100 mL of test compounds (1.25–20 mg/mL) were transferred to 96-well polystyrene microtiter plates. Following a 24-hour incubation period at 37 °C, the cells that had adhered to the wells were delicately washed with distilled water and then left to air dry. Staining was carried out with 0.4% (w/v) crystal violet in an aseptic environment and then rinsed with distilled water again. 200 mL of ethanol was used to dissolve the crystal violet. TSB medium (100 mL) was used as a negative control, and bacterial cultures without compounds were used as a positive control. The measurement of the wells was carried out at 595 nm (BioTekEpoch 2 Microplate Spectrophotometer). Anti-biofilm activity (%) was determined by the following formula. The study was repeated three times [20].

$$\text{Anti} - \text{biofilm activity } (\%) = (1 - \text{OD sample}/\text{OD control}) \times 100$$

Cell Culture and Treatment with NiONPs

SH-SY5Y human neuroblastoma cells were obtained from Gülhane Stem Cell Research Center, Health Sciences University. Cells were cultured in DMEM (Biowest, L0102-500, Nuaillé, France) containing 10% fetal bovine serum (Capricorn scientific, FBS-11 A, Germany), 1% L-glutamine and 1%penicillin/streptomycin (PSA, Gibco, 15140-122,USA) in 25 cm^2 flasks. Cells were incubated in 5% CO_2, 37 °C and appropriate humidity (PHcbi, PHC Corporation, Japan) and passaged every 2 to 3 days. When cells reached a sufficient number of cells, cell suspensions at a density of 1×10^4 cells/100 µL were seeded into 6 and 96 well plates for

experiments. After 24 h of incubation, the cells were treated with NiONPs at the concentrations determined for the study and left to incubate for 24 h. Cells not treated with NiONPs were used as control group. After incubation, kit procedures were performed according to the parameters to be analyzed.

Cell Viability Test with MTT

MTT (3-(4,5-dimethylthiazol-2-yl)−2,5-diphenyltetrazolium bromide) test was used to evaluate cell viability. Cells were seeded in 96-well plates at a density of approximately 1×10^4 cells/100 µL and incubated for 24 h to ensure that they adhere to the bottom. Then, 6.25, 9.375, 12.5, 18.75, 37.5 and 75 µg/mL NiONPs concentrations were applied to the cells and incubated for 24 h. At the end of the incubation period, 5 mg/mL MTT (Cayman Chemical, 21795, USA) solution was added to each well and the cells were incubated for another 2–4 hours at 37 °C. At the end of this period, the wells were emptied without removing the cells at the bottom. To dissolve the formed formazan crystals, 100 µL of DMSO (Emplura, Merck116743, Germany) was added to each well and shaken for 3 min, and then absorbance values at 570 nm wavelength were measured with a microplate reader (Molecular Devices Filter Max F5 ELISA Reader). Cell viability was expressed as a percentage compared to the control group.

Caspase-3 Activity Assay

Cells were seeded in 6-well plates at 1×10^6 cells/well and incubated for 24 h. After incubation, cells were treated with 4 different concentrations of NiONPs (12.5, 18.75, 37.5 and 75 µg/mL) and incubated again for 24 h. Samples were then prepared for Caspase-3 activity analysis using the Caspase-3/CPP32 Fluorometric assay kit (BioVision, Catalognumber: #K105-25, USA) following the manufacturer's analysis procedures. The prepared samples were transferred to a 96-well black plate and fluorescence values were determined in a plate reader (Molecular Devices FilterMax F5 ELISA Reader) at 360 nm excitation and 535 nm emission values. Caspase-3 activity was expressed as a percentage compared to the control group.

Analysis of Apoptosis/necrosis and Cell Cycle by Flow Cytometry

Cells were seeded in 6-well plates at 1×10^6 cells/well and incubated for 24 h. After incubation, cells were treated with 4 different concentrations of NiONPs (12.5, 18.75, 37.5 and 75 µg/mL) and incubated again for 24 h at 37 °C in a humidified, 5% CO2 incubator atmosphere. Annexin V and PI Apoptosis kit (ABP Bioscienses, Catalog number: A027, USA) was used for apoptosis/necrosis analysis of samples. After incubation, cells were trypsinized and transferred into a falcon tube. The falcon tube was centrifuged for 5 min at 300 g and the supernatant was aspirated from the medium. The pelleted cells were washed twice in cold phosphate buffered saline (Dulbecco's PBS, Capricorn, Germany) and centrifuged again. Then, the supernatant was aspirated again and the cells were resuspended in 1Xannexin binding buffer. Then, 5 µL of annexin V and 2 µL of PI were added to each 100 µL of cell suspension to stain the cells and incubated for another 15 min in the dark. After the incubation period, 400 µL of 1Xannexin binding buffer was added and mixed gently. The stained cells were analyzed by flow cytometry device (BD Accuri C6 Plus). Cell cycle analysis of the samples after 24 h of treatment with 4 different concentrations of NiONPs was performed using the CellCyclePI/RNAse kit (ABP Bioscienses, Catalog number: A056, USA) by following the steps specified in the kit. Briefly, after incubation, the cells were trypsinized (Biowest, Trypsin 0.25%-EDTA, Nuaillé, France) and placed in a falcon tube and centrifuged. Then, the supernatant was removed and washed twice with PBS and centrifuged again. Then, the resulting cell pellet was fixed in 100µL of 99% methanol kept at −20 °C for 15 min. At the end of the period, 1 mL of PBS was added and washed by centrifuging at 300 g for 3 min. Then, 0.5 mL of PI/RNAse staining solution was added to the cells and incubated at 37˚C in the dark for 30 min, and the cells were analyzed with a flow cytometry device (BD Accuri C6 Plus).

Statistical Analysis

Statistical analyses were performed using GraphPad Prism 9 software and the Social Sciences Statistics Package for Windows (SPSS) (Version 23.0; SPSS, Inc., Chicago, IL). All experiments were replicated triplicately, and the obtained data were reported as mean ± standard deviation (mean ± SD). Comparison of data with the control group was performed using a one-way ANOVA test; the Tukey test was used post-hoc in this analysis. Statistical significance was determined as $*p<0.05$, $**p<0.01$ and $***p<0.001$.

Results

Characterization of NiONPs

XRD Analysis

The X-ray diffraction (XRD) pattern of the synthesized nanoparticles is presented in Fig. 1. The diffraction peaks observed at 2θ values of approximately 36.34°, 43.22°, 62.87°, and 75.37° can be indexed to the (111), (200), (220),

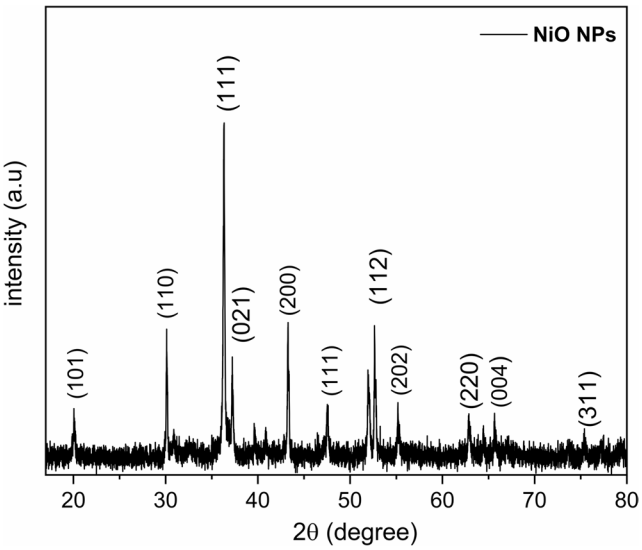

Fig. 1 XRD pattern of NiO NPs

and (311) planes of face-centered cubic (FCC) NiO, respectively, in good agreement with the standard JCPDS card No. 47–1049 and previous literature reports [21, 22]. These reflections confirm the formation of crystalline cubic NiO as the dominant phase.

Additional peaks detected at 37.25°, 47.63°, 52.59°, and 55.16° correspond to minor reflections that can be assigned to secondary nickel oxide-related phases, consistent with JCPDS card No. 14–0481 (Ni_2O_3) [21, 22]. The presence of these lower-intensity reflections indicates a small contribution from secondary nickel oxide phases within the predominantly NiO structure.

The Full Width at Half Maximum (FWHM) of the diffraction peaks provides information related to crystallite size. In this study, the crystallite size of the NiO nanoparticles was estimated using the Debye–Scherrer equation: $D = K\lambda/(\beta \cos\theta)$, where K is the shape factor (taken as 0.9), λ is the X-ray wavelength (Cu Kα, λ = 1.5406 Å), β is the FWHM of the diffraction peak (in radians), and θ is the Bragg diffraction angle. As expected, lower FWHM values correspond to larger crystallite sizes. For example, the reflection at 2θ = 30.10° (FWHM = 0.088°) yielded a crystallite size of approximately 93 nm, whereas the broader peak at 2θ = 20.08° (FWHM = 0.22°) corresponded to a smaller crystallite size of approximately 37 nm (Table 1).

The diffraction peaks selected for the calculation were intense and well-resolved to minimize peak overlap and improve the reliability of the estimation. The calculated crystallite sizes ranged between 37 and 93 nm, indicating structural heterogeneity within the synthesized NiO nanoparticles. The calculated values correspond to the size of coherently diffracting crystalline domains rather than the actual particle size. The variation in crystallite size can be attributed to differences in crystalline domain growth during synthesis. Such size distributions are commonly observed in chemically synthesized metal oxide nanoparticles due to non-uniform nucleation and growth kinetics [23, 24]. The obtained diffraction pattern is consistent with crystalline NiO, in agreement with previous reports [25].

UV–visible Analysis

The UV–Vis absorption spectrum of the NiO NPs synthesized using Kenger gum reveals a maximum absorbance of 0.961 at 400 nm, indicating strong light absorption in the UV region (Fig. 2a).This high absorbance at shorter wavelengths suggests efficient electronic transitions from the valence band to the conduction band, which is typical of semiconducting metal oxides with relatively wide optical band gaps.As the wavelength increases from 400 to 450 nm, the absorbance gradually decreases to 0.243, followed by a slower decline across the visible region.Between 670 nm and 700 nm, the absorbance stabilizes around 0.375, indicating comparatively weaker light–matter interaction in the green to red regions of the spectrum.

The transmittance spectra further support this wavelength-dependent optical behavior (Fig. 2b). The NiO NPs exhibit

Table 1 Structural parameters of NiO NPs

2θ(°)	FWHM(°)	β (radian)	Strain(ε)	Dislocation Density (ρ, nm²)	d (Å)	(hkl)	Lattice Parameter (a, Å)
20.08	0.22	0.00384	0.0394	6.7×10^{-6}	4.4	(200)	9.2
30.10	0.09	0.00153	0.0376	1.0×10^{-6}	2.9	(001)	9.6
36.34	0.13	0.00229	0.0246	2.6×10^{-6}	2.5	(311)	9.5
37.25	0.13	0.00222	0.0234	2.1×10^{-6}	2.4	(111)	9.4
43.22	0.10	0.00180	0.0189	1.3×10^{-6}	2.1	(200)	9.7
47.63	0.14	0.00244	0.0306	2.4×10^{-6}	1.9	(222)	9.9
51.94	0.15	0.00267	0.0351	2.8×10^{-6}	1.8	(200)	9.8
52.59	0.11	0.00187	0.0285	1.3×10^{-6}	1.7	(400)	9.7
55.16	0.12	0.00202	0.0325	2.4×10^{-6}	1.6	(411)	9.8
62.87	0.14	0.00243	0.0334	2.1×10^{-6}	1.5	(220)	9.9
65.63	0.13	0.00227	0.0315	1.8×10^{-6}	1.4	(521)	9.8
75.37	0.15	0.00262	0.0394	2.2×10^{-6}	1.3	(311)	10.1

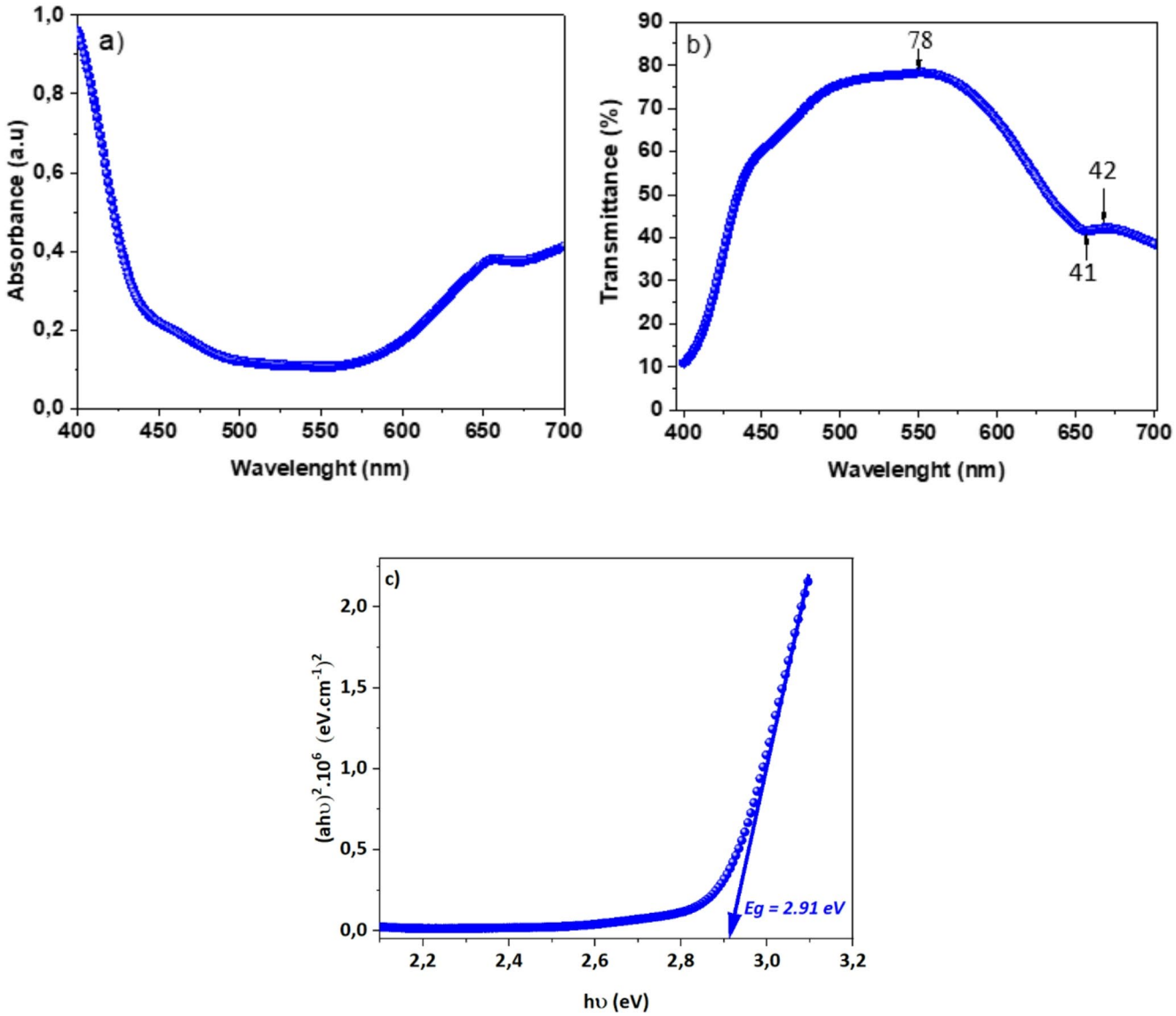

Fig. 2 **a** The UV–visible absorbance spectrum, **b** transmittance spectra and **c** bandgap values of NiO NPs

a high transmittance of 78% at 549 nm, demonstrating good transparency in the green region of visible light. In contrast, significantly lower transmittance values are observed at 656 nm (41%) and 667 nm (42%), suggesting increased absorption or scattering effects in the red region. This complementary relationship between absorbance and transmittance confirms the selective optical response of the synthesized NiO NPs.

Based on the Tauc plot analysis (Fig. 2c), the optical band gap of the NiO NPs was calculated to be 2.91 eV. The Tauc equation, $(\alpha h\nu)^n = A(h\nu - Eg)$, was used to determine the band gap, where α is the absorption coefficient, hν is the photon energy, A is a constant, Eg is the optical band gap, and $n = 2$ for a direct allowed transition. In the revised figure, the linear fitting region used to extract the band gap is clearly indicated on the Tauc plot.This value is consistent with the characteristics of wide-bandgap semiconductors and explains the relatively low absorbance and high transparency observed in the visible region. The moderate band gap indicates that the synthesized NiO NPs possess suitable optical properties for applications requiring controlled light absorption and transmission, including optoelectronic and biomedical-related technologies.

FT-IR Analysis

The FT-IR spectrum of the NiO NPs is shown in Fig. 3.The vibrational band for the metal-oxygen bond usually appears at 400 to 700 cm^{-1} in the FT-IR spectra of metal oxides [26]. Absorption bands for NiO are in the range 400–1100 cm^{-1}.The bending vibration of NiO is responsible for the

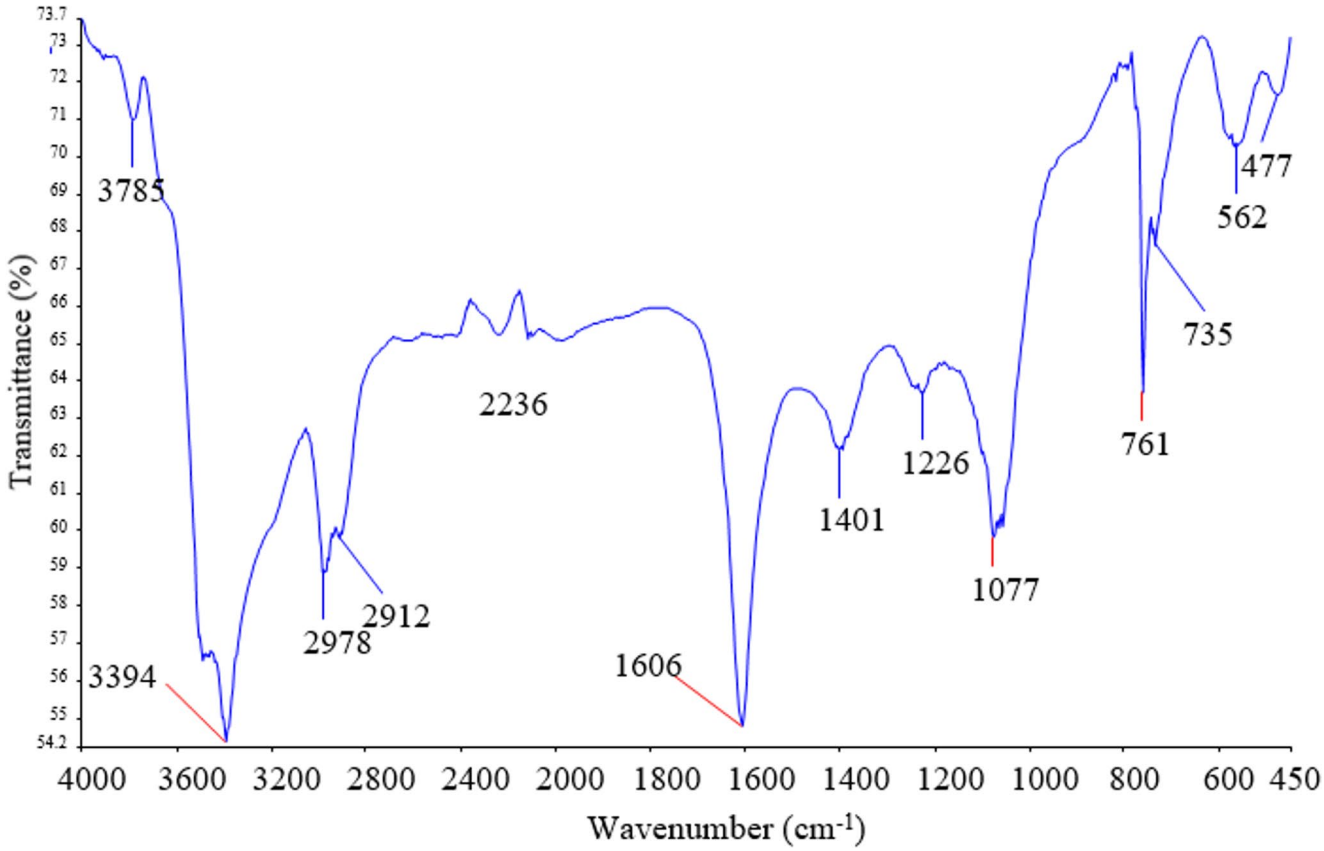

Fig. 3 FT-IR spectrum of the NiO NPs

peaks at 477, 562, 735 and 761 cm^{-1}.Typically, these bands are caused by the stretching, bending, wiggling, and other modes of vibration of the Ni-O bond [27]. Broad band at 3394 cm^{-1} assigned to chemically bound hydroxyl group and atmospheric water molecules. The band at 1077 cm^{-1} corresponds to C–O stretching vibrations, characteristic of polysaccharides and other oxygen-containing functional groups present in the gum. Less intense bands observed at 1226 cm^{-1} and 1401 cm^{-1} are indicative of minor components such as phenolic or carboxylate groups naturally present in Kenger gum, consistent with previously reported studies on mastic resin [28]. The vibration observed at 2912 cm^{-1} is probably due to the C-H stretching, while the band at 1606 cm^{-1} can be attributed to the H-O-H bending vibration band [29–31].These functional groups likely contribute to the reduction and stabilization of Ni^{2+} ions during the green synthesis of NiO NPs.

TGA/DTA and DTG Analysis

The thermal behavior of the synthesized NiO NPs was investigated using TGA, DTA, and DTG analyses, as illustrated in Fig. 4. The TGA curve reveals a total weight loss of approximately 35% over the temperature range of 30–800 °C. The initial minor weight loss below 150 °C can be attributed to the removal of physically adsorbed water molecules and moisture content. A second significant weight loss observed between 300 and 500 °C corresponds to the decomposition of organic residues or unreacted precursors remaining from the synthesis process. The DTG curve exhibits distinct peaks at approximately 150 °C, 320 °C, and a sharp peak near 700 °C, indicating the temperatures at which the maximum rate of weight loss occurs. The first peak confirms the desorption of moisture, while the second and third peaks are associated with the thermal degradation of organic compounds and the structural decomposition of the oxide, respectively. The DTA curve shows endothermic events correlating with the weight loss steps in the TGA profile. Notably, a pronounced endothermic peak is observed in the range of 680–800 °C, which can be ascribed to the release of lattice oxygen from the NiO structure. The curve shows that due to the release of bound oxygen atoms in the nanoparticles, there is a stepwise weight loss of NiO NPs at 680–800 ℃ [20].

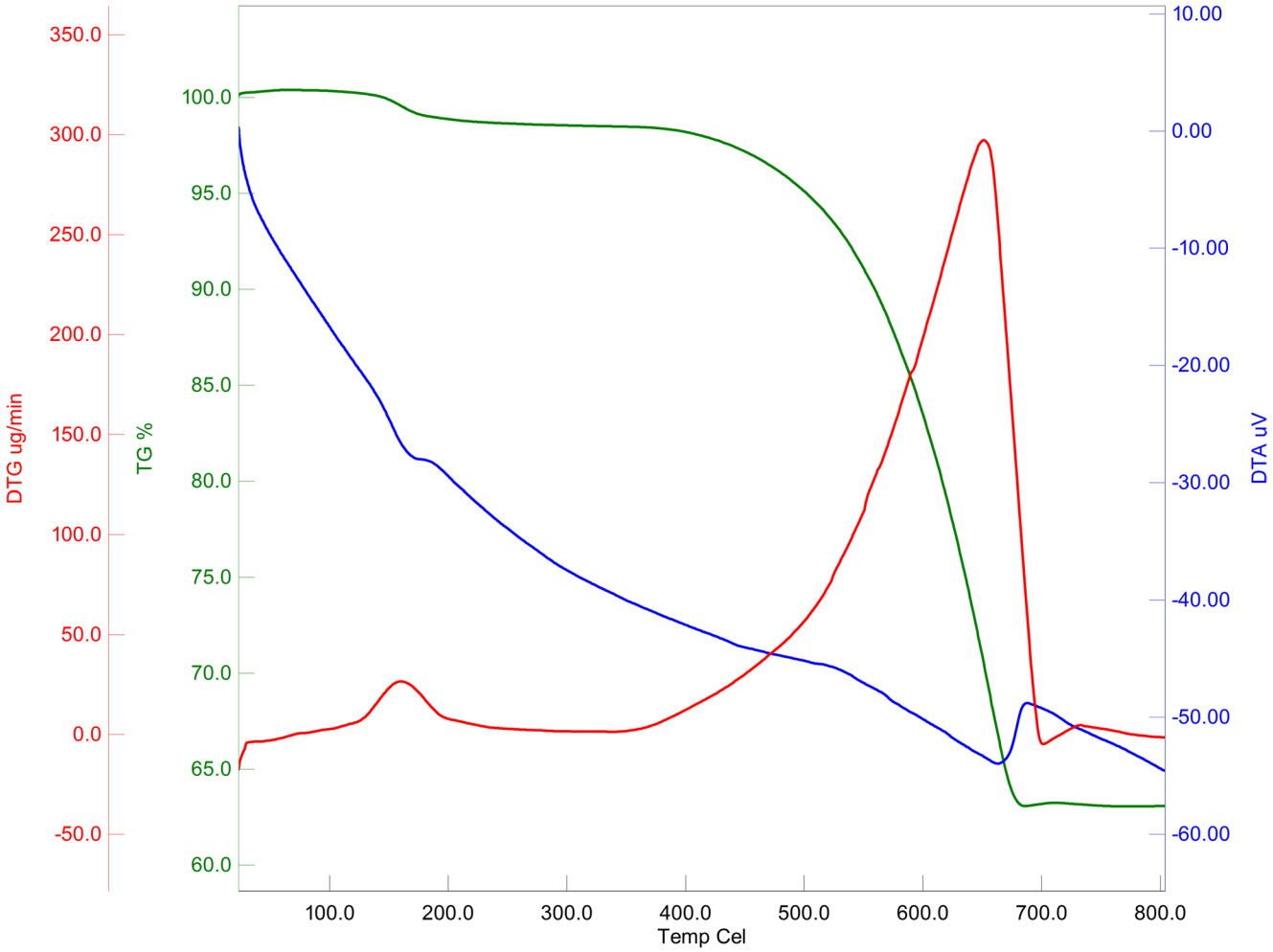

Fig. 4 TGA/DTA and DTG curves of the NiO NPs

FE-SEM Analysis

In addition to the synthesis process and biological application potential, morphological characteristics of the NiO NPs produced from Kenger gum extract were analyzed using field emission scanning electron microscopy (FE-SEM). These technique provide critical insights into the size of the nanoparticles, which are essential for understanding their behavior in biological systems.FE-SEM images of the NiO NPs are shown in Fig. 5 and were recorded at a magnification of 100.00 kx with a scale bar of 100 nm.The size of the nanoparticles is usually in the range of 20–50 nm, and their distribution can be either monodisperse (uniform in size) or exhibit some degree of agglomeration, depending on the synthesis conditions. Agglomeration, where particles cluster together due to their surface energy, is commonly observed in nanoparticles synthesized by green methods and can affect their reactivity and surface area. SEM images can also reveal interparticle interactions where particles are sometimes connected by small bridges or form larger agglomerates [32].Such morphological features, including nanoscale particle size and controlled agglomeration, are particularly advantageous for enhancing surface-related interactions, which are critical for the biological activity and functional performance of NiO NPs.The particle size distribution of the synthesized nanoparticles was evaluated based on FESEM micrographs, as illustrated in Fig. 5. The corresponding histogram reveals a relatively narrow size distribution, which can be well fitted by a Gaussian function. The average particle size was determined to be approximately 20 nm with a standard deviation (σ) of about 5 nm. This narrow distribution indicates a uniform growth process and good control over particle nucleation during synthesis. Overall, the obtained particle size distribution is in good agreement with previously reported FESEM-based size analyses for similar nanostructured systems. The particle size distribution of the synthesized nanoparticles was evaluated from FESEM images, and the corresponding histogram was constructed by analyzing the micrographs using ImageJ software.

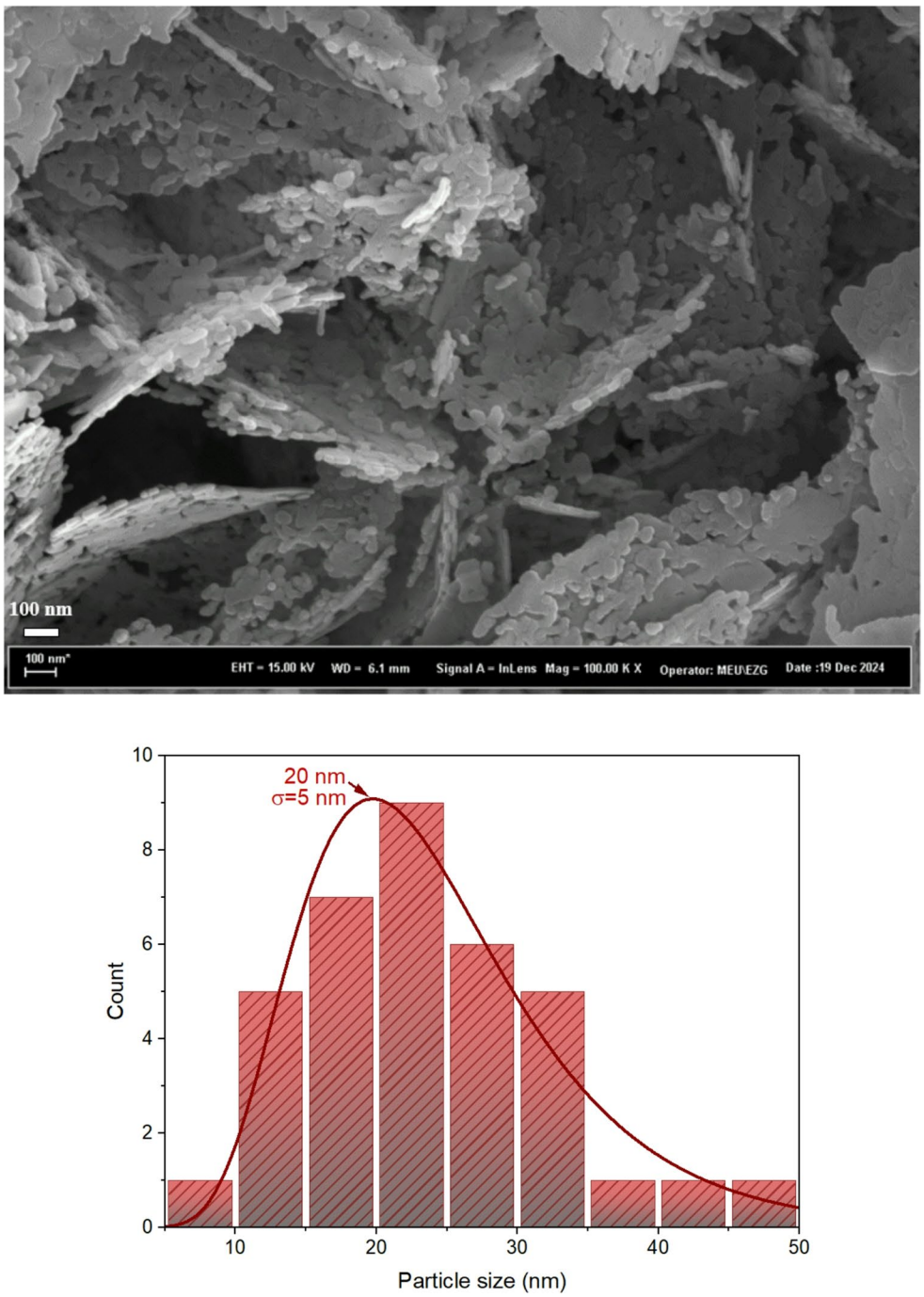

Fig. 5 FE-SEM images of NiO nanoparticles and the corresponding FESEM-based particle size distribution histogram with Gaussian fitting

Bioactivity of NiO NPs

Antimicrobial Activity

The antibacterial activity of NiO NPs was evaluated against both different reference bacterial strains and clinically important strains isolated from clinical samples. The results obtained were determined to have a particularly strong antimicrobial activity as indicated in Table 2; Fig. 6. It is important that these newly synthesized NP compounds, which were found effective on all tested strains, showed strong antimicrobial activity on clinically important and multidrug resistant *E. coli*, *P. aeruginosa* and *S. aureus*, which cause serious nosocomial infections. In particular, the high inhibitory activity on A. baumannii, which has recently become increasingly likely to be seen in hospital infections worldwide and has caused outbreaks in intensive care units, and has caused serious problems in terms of treatment due to increasing drug resistance, is remarkable [33].

Table 2 Antimicrobial zone diameters of NiO NPs on pathogenic type strains

	Antimicrobial Zone Diameter										
	Gram negative					Gram pozitive					
	EC	PA	AB	SD	KP	SA	LM	EA	EF	BC	VRE
NiONPs	31.0± 1.2	30.0±0.8	34.0±0.9	32.0±1.3	30.0±0.7	31.0±0.2	30.0±0.8	32.0±0.9	30.0±1.3	31.0±0.4	30.0±0.6
MIC [a] (µg/mL)											
NiONPs	2.0	4.0	0.5	1.0	2.0	2.0	4.0	2.0	1.0	2.0	2.0
CN [b]	0.5	1.0	0.5	0.5	1.0	0.5	0.5	0.5	0.5	1.0	0.5

EC: *E. coli* ATCC 25,922, PA: *P. aeruginosa* ATCC 27,853, AB: *(A) baumannii* ATCC 17,978, SD: *S. dysentery* ATCC 13,313, KB: *K. pneumoniae*, SA: *S. aureus* ATCC 25,923, *L. monocytogenes* ATCC 19,115, EA: *E. aerogenes* ATCC 13,048, EF: *E. faecalis* ATCC 29,212, BC: *(B) cereus* ATCC 14,579, VRE: Vancomycin resistant *E. faecium*

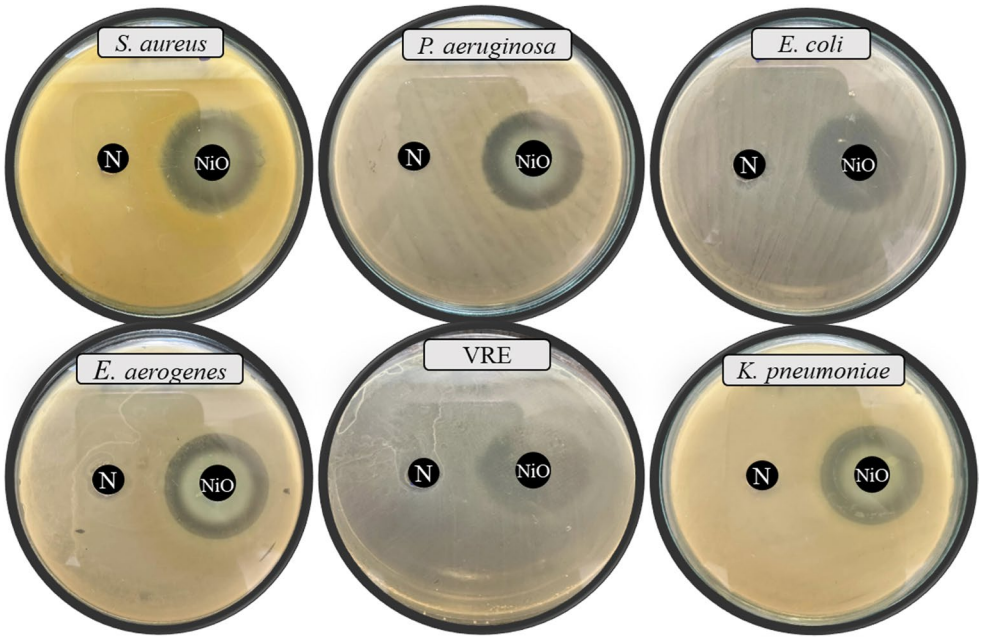

Fig. 6 Inhibition zone activities of NiO NPs on some pathogenic strains. N: Negative control

In addition to the remarkable results, when the low MIC values on the tested standard and clinical strains are compared with gentamicin used as a positive control, it is seen that the MIC values are close to each other. These results show that the newly synthesized NiONPs has the potential to be used as an alternative to antibiotics against important clinical strains.

Anti-biofilm Activity

In our study, *E. coli* ATCC 25922 and *P. aeruginosa* ATCC 27853 type strains were used to determine the anti-biofilm activity of NiO NPs. As a result of the study, it was observed that NiO NPs biofilm inhibition was high on both types of strains. It was determined that NiONPs compound showed 56.14% biofilm inhibition on *E. coli* ATCC 25922 strain and 65.23% on *P. aeruginosa* ATCC 278533 strain at a concentration of 20 mg/ml. It was determined that the antibiofilm effect of the test compounds used in the study on *P. aeruginosa* was higher than on *E. coli* strain (Fig. 7). NiO NPs exhibited activity that can be used as potential alternatives in both biomedical applications and industry due to its strong antibacterial and anti-biofilm activity.

Cell Viabilitiy and Caspase-3

The dose-dependent effects of NiO NPs on the viability of SH-SY5Y cells are presented in Fig. 8. It was found that at a concentration of 6.25 µg/mL NiO NPs, there was a significant decrease in cell viability compared to the control group ($p<0.05$). At a concentration of 12.5 µg/mL, cell viability was found to be 69.70%. A dramatic decrease in viability occurred with the increase in concentration and cell viability was found to be 39.13% at 37.5 µg/mL. It was determined that at all determined doses of NiO NPs, there was a statistically significant decrease in cell viability compared to the control group ($p<0.05$, $p<0.001$). The concentration value of NiO NPs that inhibited half of SH-SY5Y cells was found to be 23.26±0.59 µg/mL.

The changes in caspase-3 activity for four different concentration values of NiO NPs are given in Fig. 9. Partial increases in caspase-3 activity were observed in cells

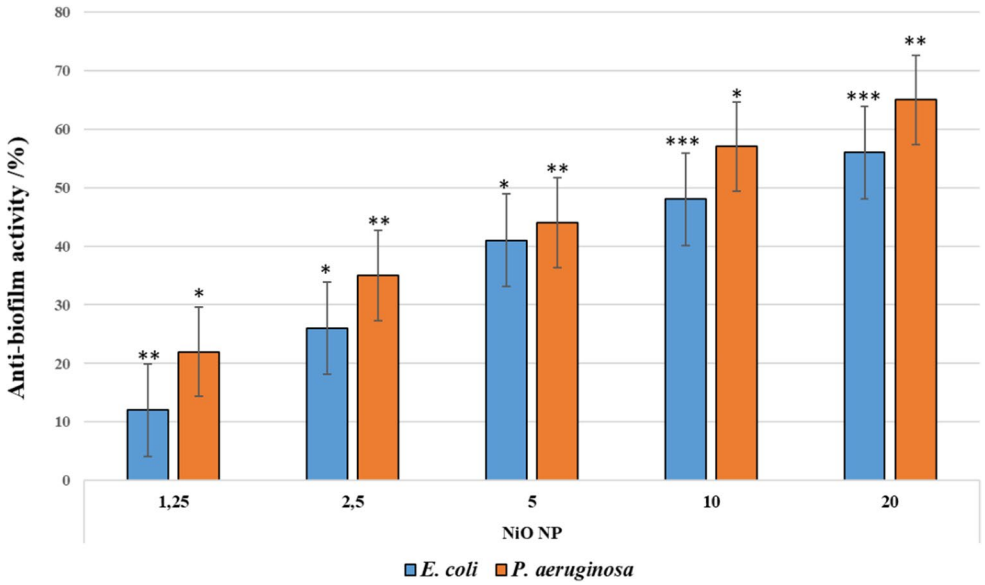

Fig. 7 Anti-biofilm activity of different concentrations of NiO NPs on *E. coli* ATCC 25922 type strain. The statistical significance values ***, **, and * denote significance at $p<0.001$, $p<0.01$, and $p<0.05$ where as ns denotes non-significance

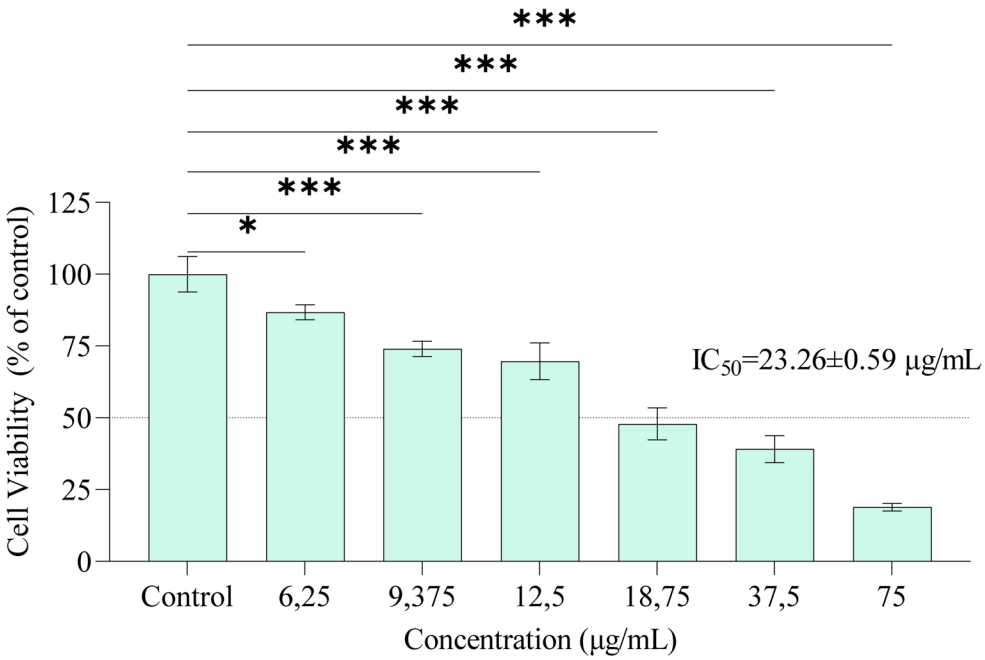

Fig. 8 Effects of different concentrations of NiO NPs on SH-SY5Y cell viability after 24 h incubation. The statistical significance values *** and * denote significance at $p<0.001$ and $p<0.05$

treated with 37.5 and 75 µg/mL concentrations. However, it was determined that these changes were not statistically significant compared to the control group ($p>0.05$). These selected doses of NiO NPs caused significant decreases in cell viability, but our results showed that cell death was not related to caspase-3 activity.

Apoptosis/necrosis and Cell Cycle

The apoptosis/necrosis states of cells treated with 12.5, 18.75, 37.5 and 75 µg/mL concentrations of NiO NPs were determined by flow cytometry and are presented in Fig. 10. 97.3% of the cells in the control group were viable cells. After treatment with 12.5 and 37.5 µg/mL concentrations, 34.7% and 43.1% of the cells were determined as necrotic cells, respectively. At the 75 µg/mL concentration, the percentage of viable cells showed a dramatic decrease and was determined as 36.4%, and in this case, 63.6% of the cells were found to be necrotic (Fig. 10). On the other hand, the effects of treatment of SH-SY5Y cells with increasing doses of NiO NPs on the cell cycle were examined (Fig. 11). It was determined that 66.4% of the cells in the control group were in the G2/M phase. After treatment with NiO NPs, a significant decrease was observed in the percentage of cells in the G2/M phase. After treatment with a concentration of 12.5 µg/mL, the percentage of cells in the G2/M phase

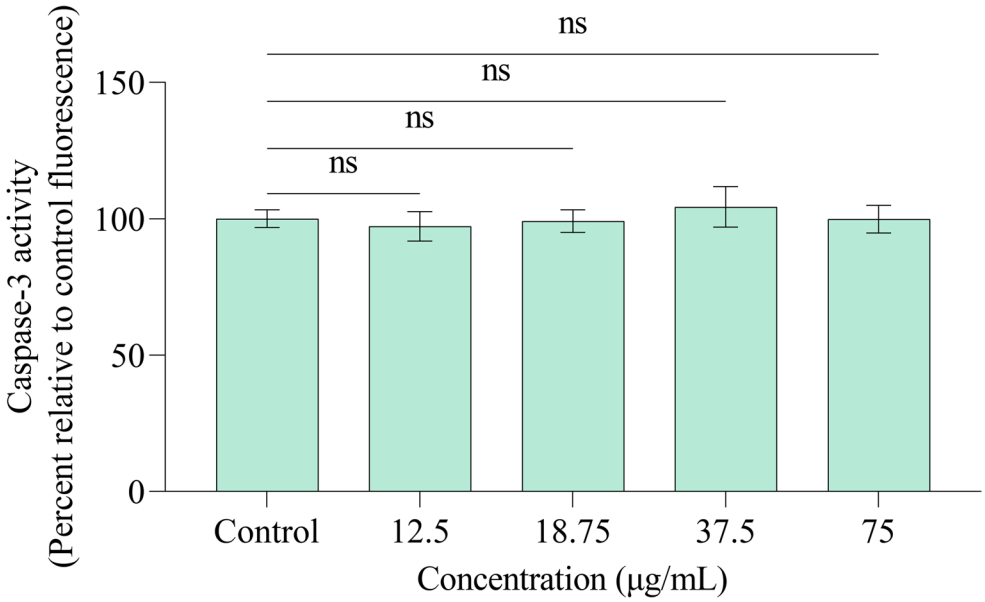

Fig. 9 Evaluation of apoptotic response in SH-SY5Y cells after 24 h NiO NPs exposure by caspase-3 activity. The statistical significance ns; denotes non-significance

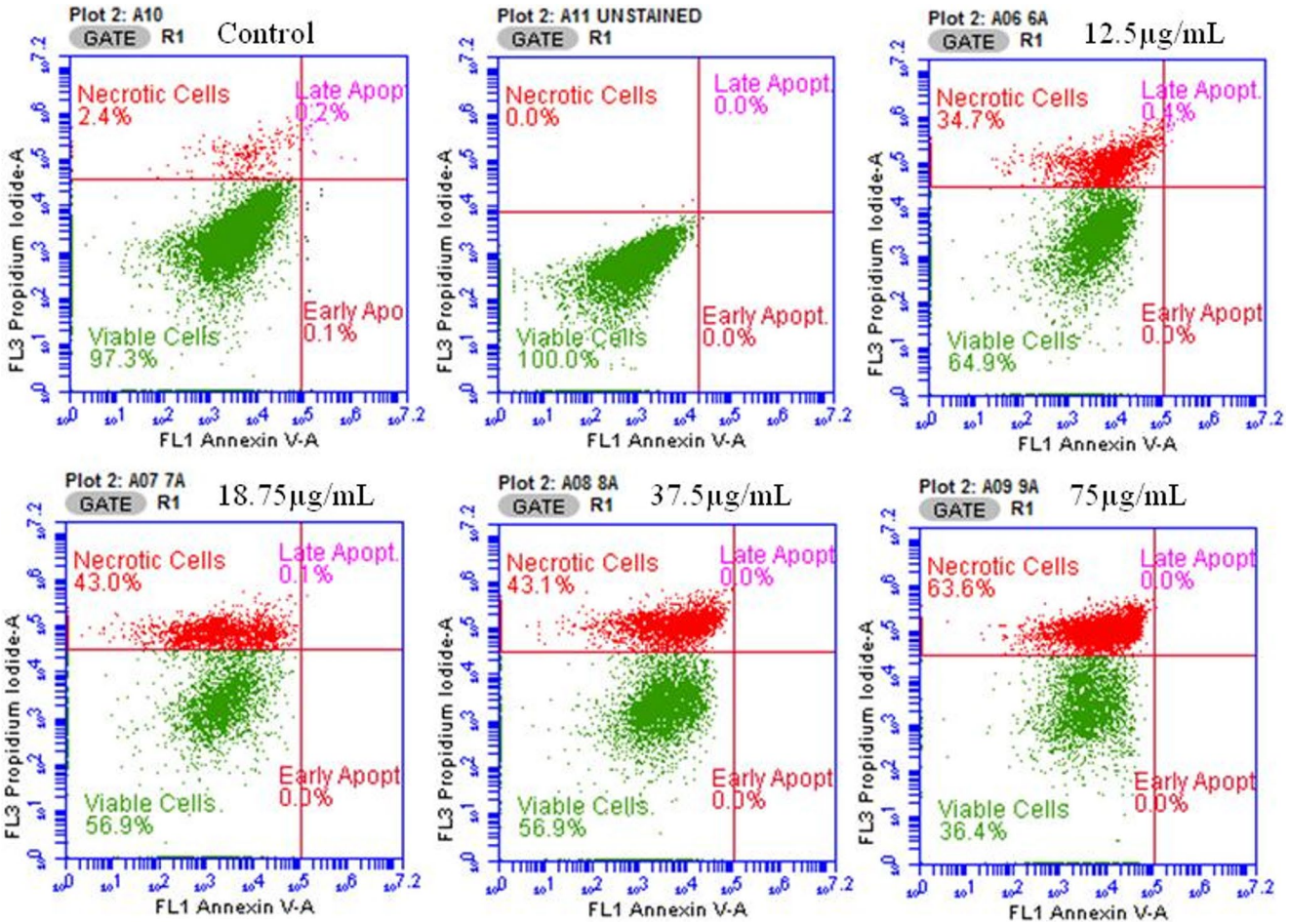

Fig. 10 Evaluation of NiO NPs-induced cell death in SH-SY5Y cells: Flow cytometric profiling of apoptotic and necrotic populations

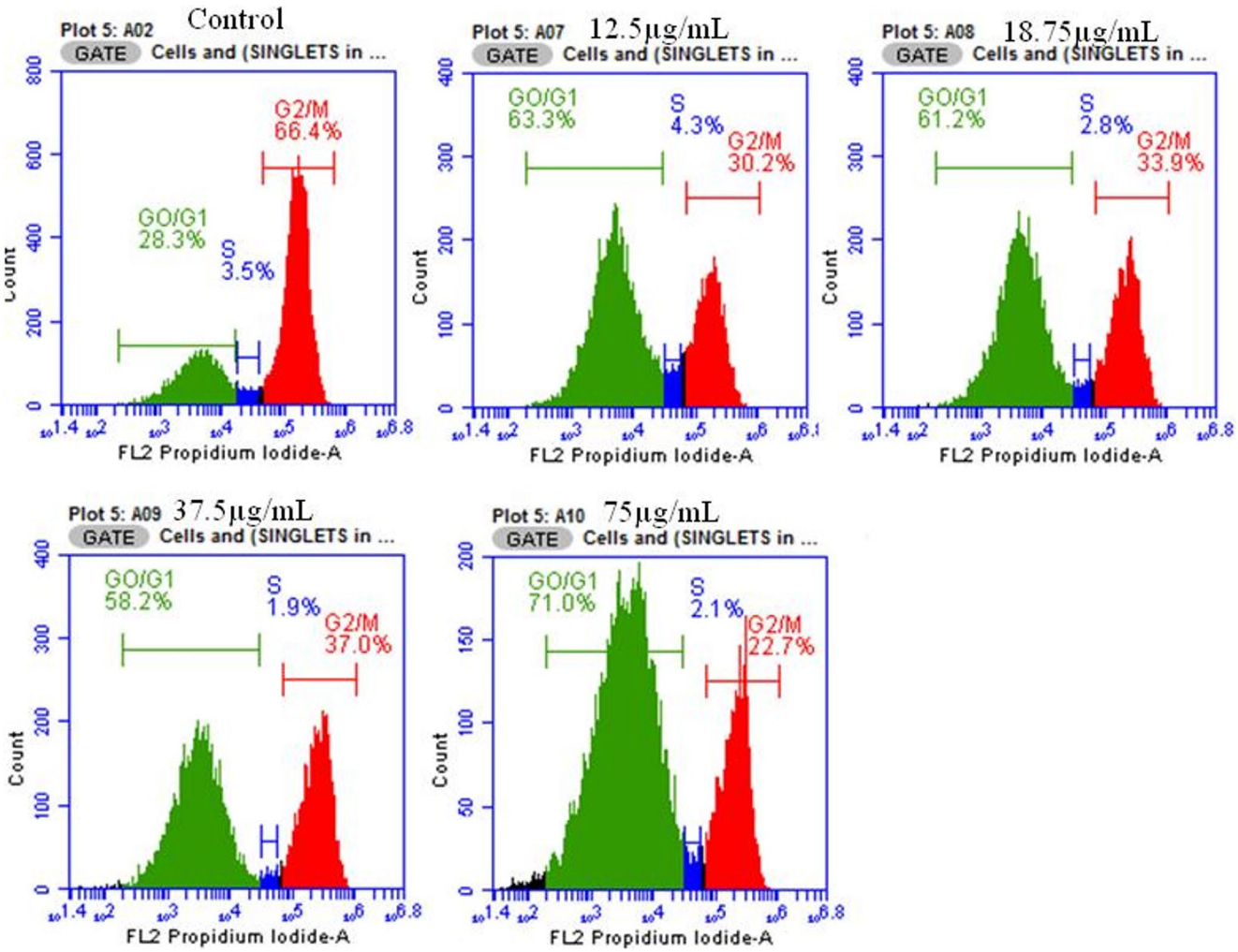

Fig. 11 Cell cycle after exposure to different doses of NiO NPs in SH-SY5Y Cells: Distribution of G0/G1, S and G2/M phases

decreased, while the percentage of cells in the G0/G1 phase was 63.3. After treatment with a concentration of 75 µg/mL, which was selected as the high concentration, it was determined that 71% of the cells were arrested in the G0/G1 phase, 2.1% were in the S phase, and 22.7% were in the G2/M phase. It was observed that NiO NPs arrested the cell cycle in G0/G1 in SH-SY5Y cells in proportion to increasing doses.

Discussion

Kenger gum is primarily composed of polysaccharides, including arabinose, galactose, xylose, rhamnose, and glucose derivatives, which contribute to its gelling, viscosity, and stability properties. Additionally, the gum contains phenolic compounds, such as phenolic acids, flavonoids, tannins, and lignans, which possess antioxidant activity by neutralizing free radicals and act as reducing and stabilizing agents during nanoparticle synthesis [34]. In this study, NiO nanoparticles (NiO NPs) were successfully synthesized using Kenger gum via a green synthesis method and characterized through XRD, UV-Vis spectroscopy, thermal analysis (TGA/DTG/DTA), and FESEM imaging. XRD patterns confirmed the crystalline NiO structure, with sharp diffraction peaks at 2θ angles of 36.34° and 43.22°, corresponding to the (111) and (200) planes, respectively, consistent with the literature [35]. UV-Vis spectra indicated their optical properties, with a band gap of 2.91 eV, confirming their semiconducting nature suitable for biomedical applications. Thermal analyses showed that the nanoparticles were stable at high temperatures [36], while FESEM revealed particle sizes ranging from 20 to 50 nm. The small and uniform particle size suggests a high surface area, advantageous for interactions in biomedical applications, including antimicrobial and anticancer activity.These findings further indicate that Kenger gum does not merely function as a passive stabilizing medium, but actively participates in

the reduction and nucleation processes through its phenolic and polysaccharide components, facilitating the controlled formation of NiO nanoparticles. Control experiments performed under identical conditions, in which either the nickel precursor or the extract was used alone, did not yield any particulate product, further supporting the essential reducing and structure-directing role of the biogenic matrix.

In a study investigating the antimicrobial activity of NiO NPs derived from polyvinyl alcohol (PVA) and aminobenzoic acid (P-ABA) derivatives by calcination method, it was reported that the nanoparticles showed antimicrobial activity against *S. aureus*, *S. epidermidis* and *E. faecalis*, *E. coli* and *P. aeruginosa* strains [37]. In another study investigating the antibacterial activity of NiO NPs synthesized using the green synthesis method using the Tribulus terrestris plant, metal ions showed significantly high activity against *E. faecalis* and *K. pneumoniae* and moderate antibacterial activity against *P. aeruginosa* [38]. The data obtained are similar to our study. Gram-positive bacteria possess a thick, negatively charged peptidoglycan layer that binds positively charged metal ions, while Gram-negative bacteria such as *E. coli*, despite having a thinner peptidoglycan layer, are generally considered less susceptible to antibacterial agents [39]. In our study, NiO NPs exhibited strong antimicrobial activity against multidrug-resistant *E. coli*, *P. aeruginosa*, *A. baumannii* and *S. aureus*. The main mechanism involves nanoparticle adhesion, leading to metal ion accumulation on the cell surface, disruption of the cell wall, and subsequent membrane damage. Studies on the antibiofilm activity of NiO NPs are limited; however, NiOx nanoparticles enriched with oxygen vacancies demonstrated strong antibacterial and antibiofilm effects against *S. aureus* in both in vitro and in vivo models [40]. It is thought that nanoparticles may be effective on biofilm formation by binding to the bacterial cell wall and preventing bacteria from adhering to surfaces.

In this study, the cytotoxic effects of green-synthesized NiO NPs on the SH-SY5Y cell line were evaluated, and the IC_{50} value was determined as 23.26 ± 0.59 µg/mL. This value is considerably lower than the IC_{50} of 229.34 µg/mL reported for chemically synthesized NiO NPs [41], indicating that the biosynthesis method can significantly enhance nanoparticle bioactivity. It has been reported in the literature that NiO NPs obtained with different herbal extracts exhibit varying levels of cytotoxic effects on various cancer cell lines. For example, NiO NPs synthesized with *Moringa oleifera* extract have IC_{50} = 125 µg/mL in HT-29 cells, while those synthesized with *Calendula officinalis* leaves have IC_{50} values in the range of 229–380 µg/mL in esophageal cancer cells [42, 43].In addition, it has been reported that this value can go up to 419.6 µg/mL for HeLa cells. [44]. These differences reveal that the plant sources and target cell types used in the synthesis play an important role in determining the cytotoxic effect. The low IC_{50}value obtained in our study indicates the high sensitivity of SH-SY5Y cells to nanoparticles and the role of the herbal source used in enhancing this effect. In addition, other studies have reported that nanoparticles obtained with different herbal extracts also exhibit dose-dependent cytotoxic effects on SH-SY5Y cells [45].This supports both the effectiveness of the biosynthesis approach and the sensitivity of the SH-SY5Y cell line to nanoparticles.

According to MTT results, NiO NPs induced a dose-dependent decrease in cell viability, indicating cytotoxicity associated with membrane damage and oxidative stress. Previous studies have reported that NiO NPs exert cytotoxic effects mainly through reactive oxygen species (ROS) generation and metal ion release, posing potential biological risks in systemic applications [16, 46, 47]. In our green synthesis-based study, NiO NPs exhibited higher cytotoxicity in HT-22 cells than in cancer cells [16]. However, it is emphasized in the literature that localized application strategies, such as intratumoral or site-specific applications, can significantly reduce systemic exposure and associated toxicity [48, 49]. Ahmad et al. demonstrated that NiO NPs caused concentration-dependent cytotoxicity associated with ROS production and G0/G1 cell cycle arrest [50]. Another study conducted with green synthesis of platinum nanoparticles reported that it caused arrest of cells in G0/G1 and G2/M phases [51]. These findings are consistent with our flow cytometry results showing G0/G1 accumulation, indicating suppressed cell proliferation. In another study by Tolliver et al., they reported that there were differences in the cell cycle according to the type of NP applied in their study with different transition metal oxide NPs [52]. Notably, no significant change in caspase-3 levels was observed, suggesting that cell death occurred via caspase-independent mechanisms. Although NiO NPs may induce apoptosis in some cell lines, this effect is not always mediated by caspase-3 [53]. Annexin V/PI analysis revealed a dose-dependent increase in necrotic cells, indicating membrane damage–related necrosis. NP-induced cytotoxicity may involve necrosis, apoptosis, or autophagy, depending on oxidative stress and cellular damage severity [54, 55]. Similarly, studies with NiO NPs have shown that they increase intracellular ROS levels and lipid peroxidation, activate oxidative stress responses, and contribute to cell damage through mechanisms that do not require caspase-3 activation [56].

In conclusion, the findings of this study suggest that the antimicrobial and anticancer activities of green synthesized NiO NPs likely occur through strong interactions with cell membranes, leading to membrane destabilization-dependent cellular damage. The predominance of necrotic and caspase-3-independent cell death suggests that mechanisms of severe cellular stress involving oxidative instability and mitochondrial dysfunction may be more prominent than classical apoptotic pathways.

Conclusion

In this study, the characterization and biological effects of NiO NPs synthesized by an environmentally friendly method using kenger gum were evaluated. Kenger gum served as both a bioreductant and a stabilizer agent in the green synthesis process and offered a sustainable alternative to traditional chemical synthesis methods. XRD analyses showed that the synthesized nanoparticles were in the form of NiO crystals with a face-centered cubic (FCC) structure in the pure phase. FE-SEM imaging revealed that the sizes of these nanoparticles were in the range of 20–50 nm.

NiO NPs obtained by green synthesis are promising in combating multidrug-resistant pathogens with their strong antimicrobial and antibiofilm activities. In addition, in vitro evaluations on the SH-SY5Y human neuroblastoma cell line determined that these nanoparticles exhibited significant antiproliferative and cytotoxic effects. It has been determined that these effects are associated with caspase-3 independent cellular damage mechanisms and lead to cell cycle arrest in the G0/G1 phase. The findings show that the biological effects of nanoparticles can vary significantly depending not only on their physicochemical properties but also on the biological agents used in the synthesis, the target cell type and the applied dose. Accordingly, it is thought that NiO NPs obtained by green synthesis method can be evaluated as potential biomaterials especially in the treatment of cancer types such as neuroblastoma. In future studies, it is recommended that the biological safety and therapeutic potential of these nanoparticles be investigated comprehensively in different cell lines and in vivo models.

Acknowledgements This manuscript used the ChatGBT artificial intelligence tool to help ensure grammatical fluency and clarity; all content was reviewed and approved by the authors.

Author Contributions ZÇ, Conceptualization, Methodology, Data curation, Investigation, Formal analysis, Supervision, Visualization, Resources, Writing - original draft, Writing - review & editing. GG, Methodology, Data curation, Investigation, Formal analysis, Supervision, Resources, Writing - original draft, Writing - review & editing. EÇ, Conceptualization, Methodology, Data curation, Investigation, Formal analysis, Visualization, Resources, Writing - original draft, Writing - review & editing. ST, Methodology, Data curation, Investigation, Formal analysis, Writing - original draft, Writing - review & editing. EK, Methodology, Data curation, Investigation, Resources, Writing - original draft, Writing - review & editing. AT, Methodology, Data curation, Investigation, Formal analysis, Writing - original draft, Writing - review & editing.

Funding Open access funding provided by the Scientific and Technological Research Council of Türkiye (TÜBİTAK). The authors declared that this study has received no financialsupport.

Data Availability The data that support the findings of this study are available from the corresponding author upon reasonable request.

Declarations

Competing Interests The authors declare no competing interests.

References

1. Berhe, M.G. and Y.T. Gebreslassie, *Biomedical Applications of Biosynthesized Nickel Oxide Nanoparticles*. Int J Nanomedicine, 2023. 18: p. 4229–4251.
2. Mathekga, K. and N.C. Hintsho-Mbita, *Synthesis of C. Benghanlensis NiO NPs for the degradation of malachite green and the removal of bacteria*. Chemical Physics Impact, 2023. 7: p. 100277.
3. Alghamdi, S.Q., et al., *High Antiparasitic and Antimicrobial Performance of Biosynthesized NiO Nanoparticles via Wasted Olive Leaf Extract*. Int J Nanomedicine, 2024. 19: p. 1469–1485.
4. Lalithambika, K., et al., *Photocatalytic and antibacterial activities of eco-friendly green synthesized ZnO and NiO nanoparticles*. Journal of Materials Science: Materials in Electronics, 2017. 28.
5. Ertuğ, F., *An ethnobotanical study in Central Anatolia (Turkey)*. Economic Botany, 2000. 54(2): p. 155–182.
6. Çoruh, N., et al., *Antioxidant capacities of Gundelia tournefortii L. extracts and inhibition on glutathione-S-transferase activity*. Food Chemistry, 2007. 100(3): p. 1249–1253.
7. Ebadi, M., et al., *Investigation the biological activities and the metabolite profiles of endophytic fungi isolated from Gundelia tournefortii L*. Scientific Reports, 2024. 14(1): p. 6810.
8. Asadi-Samani, M., M. Rafieian-Kopaei, and N. Azimi, *Gundelia: a systematic review of medicinal and molecular perspective*. Pak J Biol Sci, 2013. 16(21): p. 1238–47.
9. Haghi, G., A. Hatami, and R. Arshi, *Distribution of caffeic acid derivatives in Gundelia tournefortii L*. Food Chemistry, 2011. 124(3): p. 1029–1035.
10. al halabi, S., et al., *Phytochemical and Antiplatelet Investigation of Gundelia tournifortii*. Pharmaceutical Biology, 2008. 43: p. 496–500.
11. Karabulut, A., et al., *Comparison of the nutritive value of a native Turkish forages, tumbleweed hay (Gundelia tournefortti L.), wheat straw and alfalfa hay using in situ and in vitro measurements with sheep*. Archivos Latinoamericanos de Produccion Animal (ISSN: 1022–1301) Vol 14 Num 3, 2006. 14.
12. Abu–Lafi, S., et al., *Anticancer activity and phytochemical composition of wild Gundelia tournefortii*. Oncol Lett, 2019. 17(1): p. 713–717.
13. Dastan, D. and M. Yousefzadi, *Volatile Oil Constituent and Biological Activity of Gundelia Tournefortii L. From Iran*. Journal of Reports in Pharmaceutical Sciences, 2016. 5(1): p. 18–24.

14. Han, S., et al., *Application of silver nanoparticles containing L. leaf aqueous extract in the treatment of microbial diseases and cutaneous wound healing*. Applied Organometallic Chemistry, 2022. 36(12): p. e5491.
15. Darwish, R.M., et al., *Screening of antibiotic resistant inhibitors from local plant materials against two different strains of Staphylococcus aureus*. J Ethnopharmacol, 2002. 79(3): p. 359–64.
16. Gürsoy, G., et al., *Synthesis of NiO nanoparticles from Paulownia tomentosa plant extracts via a green synthesis method and antibacterial, antibiofilm and cytotoxicity applications*. Applied Organometallic Chemistry, 2024. 38(6): p. e7492.
17. Heng, M., et al., *Microwave-assisted green synthesis, characterization, and in vitro antibacterial activity of NiO nanoparticles obtained from lemon peel extract*. Green Processing and Synthesis, 2024. 13.
18. Kıray, E., *Antibiofilm and Anti-Quorum Sensing Activities of Vaginal Origin Probiotics*. European Journal of Biology, 2021. 80(2): p. 82–90.
19. Kowalska-Krochmal, B. and R. Dudek-Wicher, *The Minimum Inhibitory Concentration of Antibiotics: Methods, Interpretation, Clinical Relevance*. Pathogens, 2021. 10(2).
20. Theodora, N.A., V. Dominika, and D.E. Waturangi, *Screening and quantification of anti-quorum sensing and antibiofilm activities of phyllosphere bacteria against biofilm forming bacteria*. BMC Research Notes, 2019. 12(1): p. 732.
21. Barwant, M., et al., *Insights into the antioxidant and anticancer properties of novel biologically synthesized NiO/Ni2O3 nanoparticles using Sargassum tenerrimum*. Journal of Sol-Gel Science and Technology, 2024. 111.
22. Aarthi, J., et al., *Green synthesis of nickel oxide nanoparticles using leaf extract of Mimosa pudica for killing triple-negative breast cancer MDA-MB-231 cells and bacteria*. Journal of Molecular Structure, 2025. 1321: p. 140178.
23. Ahmad, W., et al., *A review on current trends in the green synthesis of nickel oxide nanoparticles, characterizations, and their applications*. Environmental Nanotechnology, Monitoring & Management, 2022. 18: p. 100674.
24. Khan, Y., et al. *Classification, Synthetic, and Characterization Approaches to Nanoparticles, and Their Applications in Various Fields of Nanotechnology: A Review*. Catalysts, 2022. 12, 1386 DOI: https://doi.org/10.3390/catal12111386.
25. Sundaresan, N., S. Ravichandran, and I. Kaliappan, *Biosynthesis of Nickel oxide nanoparticles using Evolvulus alsinoides extract and their potential photocatalytic and invitro anticancer activity*. Inorganic Chemistry Communications, 2023. 150: p. 110489.
26. Al-Zaqri, N., et al., *Green synthesis of nickel oxide nanoparticles and its photocatalytic degradation and antibacterial activity*. Journal of Materials Science: Materials in Electronics, 2022. 33.
27. Ahmad, W., et al., *A review on current trends in the green synthesis of nickel oxide nanoparticles, characterizations, and their applications*. Environmental Nanotechnology, Monitoring & Management, 2022. 18: p. 100674.
28. Venkatalakshmi, N., H. Kini, and H.S. Naik, *Green-synthesized Nickel oxide nanoparticles: Magnetic and Biomedical applications*. Inorganic Chemistry Communications, 2023. 151: p. 110490.
29. Ganesan, M., A.R. Jeice, and P. Rajaram, *Biosynthesis of NiO nanoparticles using Senna occidentalis leaves extract: Effects of annealing temperature and antibacterial activity*. Measurement: Energy, 2024. 4: p. 100023.
30. Darwich, N., et al., *Silver and Yttrium-Doped Silver Nanoparticles From Pine Needle Leaf Extract: Synthesis, Characterization, Antioxidant, Antiuropathogenic Bacterial, and Docking Activities.* Bioinorganic Chemistry and Applications, 2025. 2025: p. 1–31.
31. Darwich, N.A., et al. *Green Synthesis of Yttrium Derivatives Nanoparticles Using Pine Needle Leaf Extract: Characterization, Docking, Antibacterial, and Antioxidant Potencies*. Processes, 2024. 12, 1713 DOI: https://doi.org/10.3390/pr12081713.
32. Lin, J., et al., *In Situ Synthesis of Vertical Standing Nanosized NiO Encapsulated in Graphene as Electrodes for High-Performance Supercapacitors*. Advanced Science, 2018. 5(3): p. 1700687.
33. Ahuatzin-Flores, O.E., E. Torres, and E. Chávez-Bravo, *Acinetobacter baumannii, a Multidrug-Resistant Opportunistic Pathogen in New Habitats: A Systematic Review*. Microorganisms, 2024. 12(4).
34. Konak, M., M. Ateş, and Y. Şahan, *Evaluation of antioxidant properties of Gundelia tournefortii: a wild edible plant*. Ziraat Fakültesi Dergisi, Uludağ Üniversitesi, 2017. 31(2): p. 101–108.
35. Iqbal, A., et al., *Green Synthesis of Flower-Shaped Copper Oxide and Nickel Oxide Nanoparticles via Capparis decidua Leaf Extract for Synergic Adsorption-Photocatalytic Degradation of Pesticides*. Catalysts, 2021. 11(7): p. 806.
36. Prabha, V., et al., *Chemical synthesis of NiO nanoparticles from Solanum trilobatum leaf extract for antibacterial and cytotoxic properties*. Nano-Structures & Nano-Objects, 2024. 40: p. 101337.
37. Al-Fakeh, M.S., et al., *Nickel Oxide Nanoparticles Derived from Coordination Polymer of PVA and Aminobenzoic Acid Derivative: Synthesis, Characterization and Antimicrobial Activity*. Polymers, 2025. 17(3): p. 301.
38. Suresh, L., et al., *Phytosynthesis of Nickel Oxide Nanoparticles and Their Antioxidant and Antibacterial Efficacy Studies*. Cureus, 2024. 16(4): p. e58064.
39. Al-Fakeh, M.S., et al., *Preparation, Characterization, DFT Calculations, Antibacterial and Molecular Docking Study of Co(II), Cu(II), and Zn(II) Mixed Ligand Complexes*. Crystals, 2023. 13(1): p. 118.
40. Wang, Q., et al., *Oxygen vacancy-rich nickel oxide nanoplatforms for enhanced photothermal and chemodynamic therapy combat methicillin-resistant Staphylococcus aureus*. Acta Biomater, 2024. 182: p. 275–287.
41. Abudayyak, M., E. Guzel, and G. Özhan, *Nickel oxide nanoparticles are highly toxic to SH-SY5Y neuronal cells*. Neurochemistry International, 2017. 108: p. 7–14.
42. Ezhilarasi, A.A., et al., *Green synthesis of NiO nanoparticles using Moringa oleifera extract and their biomedical applications: Cytotoxicity effect of nanoparticles against HT-29 cancer cells*. J Photochem Photobiol B, 2016. 164: p. 352–360.
43. Zhang, Y., et al., *Green synthesis of NiO nanoparticles using Calendula officinalis extract: Chemical charactrization, antioxidant, cytotoxicity, and anti-esophageal carcinoma properties*. Arabian Journal of Chemistry, 2021. 14(5): p. 103105.
44. Abudayyak, M., O. Patan, and Ö.S. Zengin, *CYTOTOXIC AND GENOTOXIC EFFECTS OF NICKEL OXIDE NANOPARTICLES ON HeLa CELLS*. Journal of Advanced Research in Health Sciences, 2024. 7(3): p. 220–226.
45. Palei, N.N., et al., *Green Synthesis of Silver Nanoparticles of Vernonia cinerea Leaf Extract and their In vitro Cytotoxicity Activity against Neuroblastoma SHSY-5Y Cell Lines, Antimicrobial and Antioxidant Studies*. Recent Pat Nanotechnol, 2023. 17(3): p. 270–280.
46. Bai, C., et al., *Toxicity Research Progress of Nickel Oxide Nanoparticles Exposure in the Environment*. Current Pollution Reports, 2024. 10: p. 1–15.
47. Makarov, V.V., et al., *"Green" nanotechnologies: synthesis of metal nanoparticles using plants*. Acta Naturae, 2014. 6(1): p. 35–44.
48. Shi, J., et al., *Cancer nanomedicine: progress, challenges and opportunities*. Nat Rev Cancer, 2017. 17(1): p. 20–37.

49. Alexis, F., et al., *Factors affecting the clearance and biodistribution of polymeric nanoparticles*. Mol Pharm, 2008. 5(4): p. 505–15.
50. Ahmad, J., et al., *Concentration-dependent induction of reactive oxygen species, cell cycle arrest and apoptosis in human liver cells after nickel nanoparticles exposure*. Environ Toxicol, 2015. 30(2): p. 137–48.
51. Alshatwi, A.A., J. Athinarayanan, and P. Vaiyapuri Subbarayan, *Green synthesis of platinum nanoparticles that induce cell death and G2/M-phase cell cycle arrest in human cervical cancer cells*. J Mater Sci Mater Med, 2015. 26(1): p. 5330.
52. Tolliver, L.M., et al., *Differential Cytotoxicity Induced by Transition Metal Oxide Nanoparticles is a Function of Cell Killing and Suppression of Cell Proliferation*. Int J Mol Sci, 2020. 21(5).
53. Cambre, M.H., et al., *Cytotoxicity of NiO and Ni(OH)(2) Nanoparticles Is Mediated by Oxidative Stress-Induced Cell Death and Suppression of Cell Proliferation*. Int J Mol Sci, 2020. 21(7).
54. Mohammadinejad, R., et al., *Necrotic, apoptotic and autophagic cell fates triggered by nanoparticles*. Autophagy, 2019. 15(1): p. 4–33.
55. Manke, A., L. Wang, and Y. Rojanasakul, *Mechanisms of nanoparticle-induced oxidative stress and toxicity.* Biomed Res Int, 2013. 2013: p. 942916.
56. Horie, M., et al., *Evaluation of acute oxidative stress induced by NiO nanoparticles in vivo and in vitro*. J Occup Health, 2011. 53(2): p. 64–74.